Observed low cloud occurrence and boundary layer structure near the wintertime Southern Ocean sea ice margin and implications for sea ice growth

Casey J. Wall, Tsubasa Kohyama, and Dennis L. Hartmann

Department of Atmospheric Sciences, University of Washington, Seattle, Washington

Corresponding Author:

Casey J. Wall, caseyw8@atmos.washington.edu

Department of Atmospheric Sciences, University of Washington

408 ATG Building, Seattle, WA 98195-1640

Journal of Climate

Submitted June 30, 2016

Abstract

A sharp contrast in low cloud fraction and boundary layer structure across the Antarctic sea ice edge during winter is clearly detectable in active satellite retrievals, which provide an unprecedented view of high latitude clouds during winter, as well as in reanalysis products and in situ measurements. During polar winter, sea ice insulates the ocean and prevents heat and moisture transport to the atmosphere, causing the boundary layer to be convective, moist, warm and cloudy over open water, and stable, dry, cold and clear over sea ice. The average surface downward flux of longwave radiation is at least 39 W/m^2 larger over regions of open water slightly equatorward of the ice edge than over sea ice slightly poleward of the ice edge. This enhanced greenhouse effect of the boundary layer over open water slows heat loss from the ocean and horizontal expansion of sea ice. Several state-of-the-art global climate models with satellite simulators are compared to observations. Four out of seven fully coupled models simulate cloudier conditions equatorward of the sea ice edge than poleward. Other model biases are also discussed.

1. Introduction

Sea ice and marine boundary layer clouds and moisture strongly modulate high latitude climate. During winter, low clouds and moisture emit longwave (LW) radiation downward and heat the surface, while sea ice insulates the ocean and weakens ocean-atmosphere exchanges of heat and moisture. Sea ice formation in

35 the Weddell Sea affects deep water formation and the global circulation of the ocean
36 [Gordon, 1991]. Since most Antarctic sea ice lasts for less than one year, the growth
37 of sea ice during winter is an important determinant for how long the ice will persist
38 into the melt season, and hence the radiative impact it will have. Understanding of
39 high latitude climate will be improved thorough study of sea ice, low clouds, and
40 interactions between the two in the observational record, together with evaluation
41 of models against observations.

42 Satellite active remote sensing provides an unprecedented view of high
43 latitude clouds during winter. We take advantage of this new technology, as well as
44 in situ measurements and radiative transfer modeling, to examine low cloud and
45 boundary layer structure in the vicinity of the Antarctic sea ice edge. We also
46 provide a novel test for climate models based on their ability to capture the contrast
47 in low cloud on either side of the sea ice edge.

48 Interactions between sea ice and the atmospheric boundary layer have
49 previously been studied, but focus on this topic has generally been on Arctic sea ice.
50 Two exceptions are [Bromwich et al., 2012] who first pointed out that the total
51 cloud fraction observed from active satellite retrievals is ~10-20% lower in sea ice
52 covered regions of the Southern Ocean than over open water to the north, and
53 [Fitzpatrick and Warren, 2007] who used ship-based measurements of downwelling
54 shortwave (SW) radiation over the Southern Ocean to show that clouds tend to be
55 optically thicker over open water than over sea ice in austral spring and summer. In
56 the Arctic summer and early fall, low clouds have been observed to be more
57 abundant and optically thicker over open water than over sea ice from active

satellite remote sensing products [Kay and Gettelman, 2009; Palm et al., 2010] and from surface observers [Eastman and Warren, 2010]. On the other hand, [Schweiger et al., 2008] found that regions of low sea ice cover coincide with enhanced mid-level cloudiness and reduced low cloud cover in the Arctic during autumn using passive satellite retrievals. It has also been argued that boundary layer moisture (or lack thereof) triggers the onset of sea ice melt and freeze-up when advected over Arctic sea ice [Kapsch et al., 2013] and that a warmer, moister boundary layer has amplified Arctic sea ice decline in recent years [Serreze et al., 2009; Screen and Simmonds, 2010; Boisvert and Stroeve, 2015].

Most of the studies mentioned above were performed on the Arctic, while the Southern Ocean has received relatively little attention. In this study we provide, for the first time, a comprehensive analysis of low cloud and boundary layer structure near the Antarctic sea ice edge during winter.

2. Data and Methods

Cloud observations are taken from the Cloud-Aerosol Lidar with Orthogonal Polarization (CALIOP) instrument onboard the Cloud-Aerosol Lidar and Infrared Pathfinder Satellite Observation (CALIPSO). CALIOP is an atmospheric lidar that measures high vertical resolution profiles of clouds [Winker et al., 2007]. Because CALIOP is an active instrument, retrievals are not affected by low sunlight or near-surface inversions, two conditions that make retrievals of low clouds over sea ice highly uncertain or impossible with passive remote sensing techniques. As an example of the challenge of cloud detection over high latitudes with passive

instruments, [Liu et al., 2004] found that during polar night over 40% of all clouds went undetected by the cloud mask algorithm of the Moderate-resolution Imaging Spectroradiometer (MODIS) used at that time. The algorithm has since been improved, but detection of low clouds over ice covered polar regions remains a major challenge for passive instruments [Ackerman et al., 2008]. On the other hand, the signal-to-noise ratio of CALIOP is maximized in the absence of sunlight, making it well suited for studying clouds during polar night.

We use the Global Climate Model-Oriented CALIPSO Cloud Product (GOCCP) [Chepfer et al., 2010; CALIPSO, 2015], which provides monthly-mean cloud incidence on a 2°×2°×0.48 km (longitude, latitude, height) grid. For a given grid box and month, cloud incidence is defined as the number of times a cloud was positively identified divided by the total number of scenes in which the lidar was not fully attenuated above the grid box. The vertical (horizontal) resolution of CALIOP is 30 m (330 m) below 8 km and 60 m (1000 m) above, with a total of 583 vertical levels. Interpolating to the relatively coarse GOCCP vertical grid (40 levels) significantly increases the signal-to-noise ratio and provides a grid that is ideal for comparison with GCMs [Chepfer et al., 2010].

We also use observations of passive microwave sea ice concentration (SIC) from the National Snow and Ice Data Center [Peng et al., 2013; NOAA/NSIDC, 2015] and cloud liquid water path from the Multi-Sensor Advanced Climatology of Liquid Water Path dataset [Elsaesser et al., 2015]. Temperature and specific humidity fields from European Center for Medium-Range Weather Forecasts Reanalysis (ERA Interim; [Dee et al., 2011; ECMWF, 2015]) are used. All satellite and reanalysis data

analyzed are monthly-mean fields during the time period from June, 2006 to August, 2014.

Additionally, we use in situ measurements of air temperature, wind and surface energy budget terms over the Weddell Sea during winter. Temperature and wind data are taken from soundings obtained on a cruise that traversed the Weddell Sea during June-August 2013 [König-Langlo et al., 2006; König-Langlo, 2013] and surface energy budget measurements were obtained on a drifting ice floe in the western Weddell Sea during April-May 1992 as part of the Ice Station Weddell campaign [Gordon et al., 1993; Ice Station Weddell, 1993]. The soundings were taken once daily, released from a height of 10 m, and have $\sim$30 m vertical resolution in the lower troposphere. Sounding data were linearly interpolated to a vertical grid with a spacing of 30 m. A total of 50 soundings were taken poleward of 60°S, and of these soundings, half were taken between 60-65°S and half were taken poleward of 65°S. Hourly-averages of the surface heat budget measurements are analyzed. The latent and sensible heat terms were computed from eddy correlation measurements.

Finally, we use output from seven GCMs that participated in the Coupled Model Intercomparison Project Phase 5 (CMIP5) [Taylor et al., 2012], including output from the CALIPSO simulator [Chepfer et al., 2008]. Models in fully coupled and atmosphere only configurations are evaluated, and the first ensemble member for each model is used.

3. Observed winter low cloud and boundary layer structure over the Southern Ocean

3.1 Satellite Observations

Figure 1 shows 2006-2014 winter climatology of cloud incidence between 0.96-1.44 km along with the 35% SIC contour. Throughout this study the latitude of the sea ice edge is defined as the northernmost point at which the SIC is 35% at each longitude. A clear and sharp contrast in cloudiness at the 0.96-1.44 km level occurs between latitudes on either side of the ice edge, with cloud incidence generally ~30% over open water and ~10% over ice. The gradient of cloud incidence across the ice edge is weakest in the Western Pacific and Southern Indian Ocean (20°E – 160°E) where the ice edge is closest to shore. Further analysis is carried out over the Weddell and Ross Seas (defined as 50°W-0°E and 130°W-170°E, respectively; Figure 2) where the ice edge is farthest offshore.

We now consider the vertical profile of cloudiness, temperature and humidity in the lower troposphere. For each gridpoint and time (only monthly-means from June, July and August (JJA) between 2006-2014 are considered), the meridional distance between the gridpoint and the ice edge was computed. Data were then composited by meridional distance from the ice edge in bins of width 0.5° latitude, and the mean of each bin computed. This procedure was also done on the JJA-mean of each year, and the main conclusions are the same using either monthly or seasonal averages.

Figure 2b and 2f show the vertical profiles of mean cloud incidence in the lower troposphere as a function of meridional distance from the sea ice edge in the Weddell and Ross Seas, respectively. The boundary layer is, on average, deeper and cloudier equatorward of the sea ice edge than poleward. The mean total low cloud fraction (LCF), defined as cloud fraction below the 680 hPa level (~3.2 km), as well as the mean SIC are shown in Figure 3c and 3g (see Appendix). The mean SIC can be split into three regions: an "ice" zone in which SIC~100% that occurs poleward of 2° south of the ice edge, an "open water" zone in which SIC~0% that occurs equatorward of 1° north of the ice edge, and a "transition" region between. The mean LCF in the "ice" zone is 50% to 55% and bins within the "ice" zone have a nearly uniform LCF to within the 95% measurement uncertainty. This is also true for the "open water" zone, where mean LCF is 65% to 70%. The mean LCF is significantly larger in the "open water" zone than the "ice" zone (i.e. there is no overlap between the 95% confidence interval of any bin in the "open water" zone with any bin in "ice" zone). Across the "transition" zone, LCF increases smoothly as SIC decreases.

Finally, vertical profiles of mean potential temperature and specific humidity from reanalysis as a function of meridional distance from the ice edge are shown in Figure 3d and 3h. The boundary layer is clearly more stable over sea ice than over open water, as can be seen by the vertical spacing in the potential temperature contours. Near the surface, temperatures are close to the freezing temperature over open water and drop more rapidly poleward of the ice edge. Boundary layer specific

168 humidity values are also nearly a factor of two larger over open water than over sea
169 ice.

170 **3.2 Ground-based Observations**

171 **a. Boundary layer vertical structure from soundings**

172 Soundings can resolve the vertical structure of the boundary layer and
173 provide further insight into the physical process at work. We analyze soundings
174 taken from a cruise that traversed the Weddell Sea during June-August 2013 [König-
175 Langlo, 2013]. The cruise track is shown in Figure 3.

176 We begin with a brief description of sea ice in the Weddell Sea during
177 midwinter as observed from cruises. The sea ice edge is typically found between 60-
178 65°S and advances northward by several degrees latitude over the course of the
179 winter (Figure 1). Near the outer edge of the sea ice there is a ~250 km north-south
180 band of fragmented pancake ice with pockets of exposed seawater. Farther south,
181 sea ice is organized into vast floes that cover the ocean surface nearly completely
182 [Wadhams et al., 1987, their Figure 12]. Sounding data is composited into
183 measurements made between 60-65°S and poleward of 65°S. It is likely that many of
184 the soundings obtained between 60-65°S were taken above or close to regions of
185 open water, either within the band of fragmented pancake ice or north of the ice
186 edge, and the soundings poleward of 65°S were taken over consolidated pack ice.

187 Figure 4 shows the probability density function of temperature at each
188 height recorded by the soundings between 10-1500 m. This was computed by
189 binning the data at each level into bins of width 2°C, computing the frequency of

occurrence of each bin, and normalizing by the number of soundings. Clear bimodality in the soundings between 60-65°S is seen, which illustrates the influence of sea ice on the boundary layer structure. The warm mode closely follows a moist adiabat with a surface temperature of -1.8°C, the approximate freezing temperature of seawater in the Southern Ocean. This warm mode forms where the atmosphere is in contact with open water, and under such circumstances the boundary layer is convective and moist. Only the cold mode is found poleward of 65°S because the presence of sea ice diminishes the heat and moisture fluxes to the atmosphere. Low-level inversions are common in the cold mode (e.g. Figure 5).

Low-level jets are also frequently seen in the soundings, indicating the presence of a stable boundary layer (Figure 5). A low-level jet is defined as a local maximum in wind speed of at least 2 m/s that is below 1 km. Low-level jets exist above stable boundary layers and, at least in temperate latitudes, are initiated when the boundary layer transitions from convective to stable. The sudden shoaling of the boundary layer during this transition causes a reduction in drag from turbulent momentum flux, and therefore a sudden increase in wind speed, at heights above the stable boundary layer but below the former convective boundary layer top. At these heights the wind undergoes inertial oscillations that are nearly undamped because of the stable boundary layer below, and wind speeds can therefore exceed geostrophic values [Blackadar 1957; Thorpe and Guymer, 1977].

Low-level jets were identified in 31 of the 50 soundings taken poleward of 60°S. The low-level jets tend to be oriented toward the north west and west, and within the jet core, wind speeds in excess of 15 m/s are not uncommon (Figure 5).

213 The mechanism that initiates low-level jets over Antarctic sea ice during winter is
214 not fully understood. Low-level jets were identified at locations throughout the
215 cruise, but were especially prevalent near the Antarctic Peninsula (not shown),
216 suggesting that some of the observed jets are driven by outflow from the barrier
217 winds in the western Weddell Sea. The barrier winds are strong, low-level winds
218 that parallel the mountain range on the Antarctic Peninsula, and are driven by a
219 pressure gradient that develops when low-level easterly flow across the southern
220 Weddell Sea is obstructed by the mountains on the Antarctic Peninsula
221 [Schwerdtfeger, 1973; Parish, 1983]. It has been hypothesized that, away from the
222 influence of the barrier winds, low-level jets over sea ice are initiated by advection
223 of air from the convective boundary layer that forms above open water. This warm
224 advection may temporarily deepen the boundary layer and erode the low-level jet.
225 Then the air mass cools, a stable boundary layer forms, and a new low-level jet is
226 initiated [Andreas et al., 2000]. Katabatic winds may also drive low-level jets near
227 the Antarctic coast.

228 **b. Surface energy budget over sea ice in the Weddell Sea**

229 The surface energy budget must be examined in order to understand the
230 extent to which the boundary layer influences the development of Antarctic sea ice.
231 We analyze surface energy budget measurements taken on a drifting ice floe called
232 the Ice Station Weddell during April-May 1992 [Gordon et al., 1993]. The drift path
233 is shown in Figure 3. It is important to bear in mind that the Ice Station Weddell
234 measurements were made in the interior of the Weddell Sea over a thick slab of

multi-year ice for only two months in early winter, and therefore may not be representative of the Southern Ocean as a whole.

The surface heat budget measurements are shown in Figure 6, and are dominated by the LW fluxes. The net flux is typically negative, indicating heat loss from the ice. To leading order, the heat loss is balanced by upward conduction of heat that is released at the ice-ocean interface as seawater freezes, and by heat supplied from the ocean [Thorndike, 1992]. Comparison of the LW fluxes reveals that heat loss from the ice is an order of magnitude larger when the downward LW flux is relatively small (i.e. when the boundary layer is clear, cold and dry) than when the downward LW flux is large (i.e. when the boundary layer is warm, cloudy and moist). This can be seen by comparing the red and black lines in Figure 6b. The red line shows the mean surface downward LW flux as a function of upward LW flux, which was computed by binning the data by downward LW flux into bins of width 10 Wm^{-2} and then computing the mean upward LW flux and 95% confidence interval for each bin. The confidence interval has been adjusted to account for serial correlation of the data [Bretherton et al., 1999; their equation 31]. In the Arctic winter, the net surface LW flux over sea ice also has bimodal behavior, with a preferred value of ~-40 W/m^2 under clear skies or thin ice clouds and ~0 W/m^2 during cloudy conditions [Stramler et al., 2010].

The net surface heat flux is an important determinant of the rate of sea ice thickening during winter. On seasonal timescales, there is approximate heat balance in the sea ice between heat flux to the atmosphere (F_{atm}) and ocean (F_{ocn}) and latent heating from the formation of new ice:

$$-L\frac{dh}{dt} \approx F_{atm} + F_{ocn}$$

where $L = 3{\times}10^8$ J/m^3 is the latent heat of fusion of sea ice, h is the sea ice thickness, and F_{atm} and F_{ocn} are defined to be positive when heat flows into the ice. We neglect heat storage within the ice because, on seasonal timescales, it is much smaller than latent heating from the formation of new ice [Thorndike, 1992]. Horizontal heat transport is also neglected.

The observed net surface heat loss to the atmosphere has a mean value of $F_{atm} = -19.0 \pm 0.5$ Wm^{-2} for clear and dry conditions (defined as scenes in which the downward LW flux is less than 200 Wm^{-2}) and $F_{atm} \approx -8.0 \pm 0.5$ Wm^{-2} for cloudy and humid conditions (defined as scenes in which the downward LW flux is greater than 200 Wm^{-2}). Using the heat balance described above, this implies that the mean ice growth rate is approximately 3 mm/day larger for clear and dry conditions than for cloudy and humid conditions, assuming the same ocean heat flux. Since Antarctic sea ice typically reaches a thickness of ~0.5 m by the end of growth season [Kurtz and Markus, 2012], these observations suggest that temperature and moisture advection over sea ice can substantially reduce ice thickness on seasonal timescales.

4. Computing surface downward LW flux near the sea ice edge

The surface energy budget measurements taken from Ice Station Weddell provide valuable insight into the energetics of Antarctic sea ice growth, but are very limited in both space and time. It remains to be seen whether or not there is a jump in surface downward LW flux across the sea ice margin due to differences in boundary layer properties on either side of the ice edge, and if so, if the difference in LW flux is large enough to influence the horizontal expansion of sea ice during winter. We examine this question using the one-dimensional Rapid and Accurate Radiative Transfer Model for GCMs [Mlawer et al., 1997; Clough et al., 2005; Iacono et al., 2008] forced with atmospheric temperature and humidity profiles from reanalysis and cloud liquid water path (LWP) from satellite observations over the Weddell Sea during JJA.

In order to examine the winter surface energy budget on either side of the sea ice edge we again sort data into an "open water" and "sea ice" composite, defined as all scenes 1°-3° equatorward and 2°-4° poleward of the ice edge, respectively. Sea ice cover in the "open water" ("sea ice") region is approximately zero (complete) (Figure 2c). The temperature and humidity profiles for the "open water" and "sea ice" composites are shown in Figure 7. The profiles are characterized by a relatively cold, stable and dry boundary layer over sea ice and a warm and moist boundary layer over open water, which is qualitatively in agreement with the soundings presented earlier. The model was run with all profiles of temperature and humidity during the period of study.

298 We also compute the surface LW cloud radiative effect for low clouds, which
299 we call LW CRE*, defined as the difference in surface downward LW flux with a low
300 cloud present and with clear-sky conditions. A positive value of LW CRE* indicates
301 that low clouds have a warming effect on the surface. The asterisk is meant to
302 remind the reader that we compute the surface LW cloud radiative effect at a point
303 beneath a low cloud that covers the sky. In other words, if a low cloud suddenly
304 passes overhead and covers the sky, then LW CRE* is equal to the additional LW flux
305 reaching the surface. LW CRE* is generally not equal to the monthly mean LW CRE
306 because only low clouds are considered in the calculation of LW CRE* and, at a given
307 point, low clouds will not obscure the sky for the entirety of the month. The
308 calculations were performed without middle or high clouds in order to isolate the
309 contribution to the surface energy budget made by low clouds.
310 We make several assumptions about low clouds in the calculations. We use
311 satellite observations of LWP for the "open water" composite and use a wide range
312 of liquid and ice cloud conditions for the "sea ice" composite where observations are
313 not available. Low clouds are assumed to have a base at 0.5 km and a top at 1 km.
314 Uncertainty in the LWP retrievals over the "open water" composite is less than 10
315 g/m^2 for all observations considered and is typically ~4 g/m^2. Uncertainty in LWP
316 has a negligible effect on the computed surface downward LW flux because liquid
317 clouds are nearly opaque to LW radiation for LWP values greater than ~20 g/m^2,
318 which is much lower than values observed over the Southern Ocean (Figure 7c)
319 [Hartmann, 2016]. Low clouds over "open water" are assumed to consist entirely of
320 supercooled liquid, which is a good approximation over the Southern Ocean [Hu et

al., 2010; Morrison et al., 2011], and have a droplet effective radius of 16 μm, which is close to the observed wintertime mean over the Southern Ocean [McCoy et al., 2014, their Figure 9].

The clear-sky surface downward LW fluxes are significantly larger over "open water" than over "sea ice" because of the warmer, moister boundary layer (Figure 8). The average downward LW flux at the surface is 24.4 W/m^2 larger over "open water" than over "sea ice" and the difference is significant at the 95% confidence level. In order to test the sensitivity of the surface downward LW flux to variations in humidity and temperature, the calculations were repeated with humidity fixed to mean values at each height and temperature varied, and vice versa. The clear-sky surface downward LW flux is slightly more sensitive to variations in temperature than to variations in humidity (not shown).

Low clouds make a substantial contribution to the surface downward LW flux. The mean surface LW CRE* over the "open water" region is 87.3 $\pm$ 0.1 Wm^{-2}, which is a 44% increase over the clear-sky surface downward LW flux (Figure 8). The surface LW CRE* is insensitive to variations in LWP because liquid clouds become nearly opaque to LW radiation at LWP values of $\sim$20 g/m^2, which is much lower than observed values over the "open water" composite (Figure 7c). The 95% confidence interval for the mean LW CRE* over open water is therefore quite narrow and can hardly be seen in Figure 8b.

Differences in the mean boundary layer properties over the "sea ice" and "open water" composites can be used to compute the jump in surface downward LW

flux across the sea ice margin. Mean values for the quantities needed for this calculation are shown in Table 1.

The average surface downward longwave flux ($LW_{\downarrow}$) can be expressed as the sum of the clear-sky flux ($LW_{\downarrow,clear}$) and the additional surface downward LW flux contributed by a low cloud (LW CRE*) multiplied by the frequency at which low clouds are observed (LCF):

$$LW_{\downarrow} = LW_{\downarrow,clear} + LCF(LW\ CRE^{*}).$$

This equation neglects the contribution of middle and high clouds to the surface energy budget. However, middle and high cloud fractions are much smaller than the mean LCF and are not significantly different between the "sea ice" and "open water" composites (not shown). If Δ represents the difference of a quantity across the sea ice edge, then

$$\Delta LW_{\downarrow} = \Delta LW_{\downarrow,clear} + \Delta LCF(LW\ CRE^{*}) + LCF(\Delta LW\ CRE^{*}) + O(\Delta^{2}).$$

In other words, the jump in surface downward LW flux across the sea ice edge is due to differences in clear-sky LW flux, low cloud frequency of occurrence, and radiative properties of low clouds. The first and second term on the right hand side, which correspond to the contribution from the difference in clear-sky LW flux and from differences in low cloud occurrence, are 24 W/m^2 and 15 W/m^2, respectively. The third term, which is the contribution from differences in radiative properties of low

clouds across the ice edge, cannot be computed due to lack of observations of cloud liquid and ice water path over sea ice. However, the average surface LW CRE over the "open water" composite is at least as large, if not larger, than over "sea ice" (Figure 8b). Neglecting the contribution from higher order terms, it follows that the average surface downward LW flux is at least 39 W/m^2 larger over the "open water" region than over "sea ice." We emphasize that we have computed a lower bound estimate for the jump in average surface downward LW flux across the sea ice edge during winter. Our estimate accounts for differences in low cloud occurrence across the sea ice margin but not for differences in the radiative properties of low clouds. If low clouds over sea ice are more often composed of ice due to colder temperatures, or tend to hold less condensate because of their shallower depths (Figure 2b), then the true value for the jump in mean surface downward LW radiation may be on the order of 10's of W/m^2 larger than our lower bound estimate of 39 W/m^2 (Figure 8b).

Suppose that the clear and cold boundary layer that forms over sea ice was able to persist over open water, so that heat loss from the ocean was $\Delta \mathrm{LW}_{\downarrow} = 39$ W/m^2 larger. Assuming an ocean mixed layer of depth $h_{ML} = 100$ m [Dong et al., 2008], this additional heat loss would cool the mixed layer at a rate of

$$\frac{dT}{dt} = \frac{\Delta \mathrm{LW}_{\downarrow}}{c_p \rho_w h_{ML}}$$

where $c_p = 3985$ J/(kg °C) is the heat capacity of seawater at 0°C and $\rho_w = 1024$ kg/m^3 is the density of seawater at salinity of 30 g/kg. Over a 30 day period, this would result in a cooling of the mixed layer of 0.25°C. If this additional heat loss were instead used to freeze new sea ice, it would cause a growth rate of:

$$\frac{dh}{dt} \approx \frac{\Delta \mathrm{LW}_{\downarrow}}{L}$$

which would result in 0.34 m of sea ice over a 30 day period. The strong greenhouse effect of the convective boundary layer over open water therefore acts to slow heat loss from the ocean and horizontal expansion of sea ice.

5. Southern Ocean winter low cloud in Global Climate Models

Accurate representation of marine boundary layer clouds and their radiative effects has long been recognized as a major challenge for global climate models (GCMs) [Dufresne and Bony, 2008; Trenberth and Fasullo, 2010]. We provide a brief evaluation of several GCMs based on their ability to simulate the contrast in low cloud amount across the sea ice edge. Both fully coupled and atmosphere only (AMIP) configurations are analyzed between 1990-2004 [Taylor et al., 2012; Gates, 1992]. Fully coupled models have prescribed radiative forcing from observations, while AMIP models have prescribed sea surface temperature and sea ice concentration from observations. Model climatologies are compared to the climatology from observations taken between 2006-2014.

406 Figure 9 shows the JJA-mean 0.96–1.44 km cloud incidence and sea ice edge
407 over the Southern Ocean for seven fully coupled CMIP5 models and observations.
408 Model behavior is quite diverse; some models simulate slightly cloudier conditions
409 over sea ice than over open water (i.e. the IPSL models) and others simulate a
410 gradient in total low cloud fraction across the sea ice edge that is roughly a factor of
411 three larger than observations (e.g. MIROC-ESM-CHEM and MIROC-ESM; Figure 11).
412 Four of the seven fully coupled models simulate cloudier conditions over open
413 water than over sea ice in the vicinity of the sea ice edge, with the two IPSL models
414 and the MPI model being the exceptions. The MPI model does simulate a deeper low
415 cloud layer over open water than over sea ice, but also simulates far too much cloud
416 over sea ice in the lowest model layer (not shown). The IPSL models differ only in
417 resolution and have very similar climatological profiles of LCF and the sea ice edge
418 (Figure 9; Figure 11). Finally, it is interesting to note that in observations, the
419 magnitude of the gradient in low cloud incidence across the ice edge at the 0.96-1.44
420 km level is smallest in the Western Pacific and Southern Indian Ocean (20°E–160°E),
421 and models do not capture this pattern.
422 Results from the atmosphere only models are shown in Figure 10. In this
423 configuration, sea ice can influence the boundary layer above but not vice versa. All
424 models except for CNRM-CM5 have a clear jump in cloud cover across the ice edge in
425 the layer between 0.96-1.44 km, demonstrating the influence of sea ice on the
426 boundary layer in models. Model bias in mean LCF across the ice edge is smaller in
427 the atmosphere only models than in the fully coupled models (Figure 11),
428 suggesting that problems with ocean models, sea ice models, or coupling between

429 the two and the atmosphere may contribute additional bias in low cloud. It will be
430 useful to see if this is true for a larger set of GCMs when satellite simulator output
431 for more models becomes available.

432 6. Conclusions

433 Active satellite retrievals from CALIPSO and in situ measurements show a
434 strong contrast in low cloud amount and boundary layer structure over Antarctic
435 sea ice and the adjacent open ocean during winter. Sea ice insulates the ocean,
436 causing a cold, stable, dry and clear boundary layer to form over sea ice and a warm,
437 cloudy, moist and convective boundary layer over open water. On average, the
438 surface downward LW flux is at least 39 W/m^2 larger over open water north or the
439 sea ice edge than over sea ice to the south. The relatively strong greenhouse effect of
440 the convective boundary layer that forms over open water slows cooling of the
441 ocean mixed layer and sea ice growth compared to what would happen if the clear,
442 dry boundary layer that forms over sea ice was able to persist over open water.
443 Similarly, advection of moist boundary layer air from open water regions to sea ice
444 covered regions slows sea ice growth.

445 These results support the hypothesis of two way interactions between the
446 ocean surface and the atmospheric boundary layer during winter over high latitude
447 oceans. Regions of open water have relatively warm surface temperatures and large
448 surface fluxes of heat and moisture to the atmosphere. Moist, warm, and convective
449 boundary layers with a strong greenhouse effect form over open water and thus
450 reinforce the warm surface temperatures there. If such a region were to become

451 covered by sea ice then the surface heat and moisture fluxes would dramatically
452 reduce and the boundary layer would cool, dry and radiate less LW down to the
453 surface. This would reinforce the cool surface temperatures and allow the sea ice to
454 persist. Interactions between the ocean, sea ice and the boundary layer have been
455 proposed as a positive feedback in response to Arctic sea ice loss [Serreze et al.,
456 2009; Kay and Gettelman, 2009; Screen and Simmonds, 2010], to influence natural
457 variability in the present Arctic climate [Leibowicz et al., 2012] and as a mechanism
458 to explain equable climates [Abbott and Tziperman, 2008]. Over the Southern Ocean
459 during winter, interactions between the ocean, sea ice, and atmospheric boundary
460 layer act to reinforce the relatively warm temperatures over open water and cold
461 temperature over sea ice, and hence to stabilize the location of the sea ice edge.
462 Additionally, seven CMIP5 models with CALIPSO simulator output were
463 examined. This work highlights the large differences in the mean profiles of low
464 clouds over ocean in GCMs. We hope that the observed relationships shown here
465 will be a useful test for future model intercomparison projects when CALIPSO
466 simulator output for more models is available.
467

Acknowledgements

This research was conducted with support from NASA grant NNX14AJ26G, Terra and Aqua Science. Tsubasa Kohyama was supported by the National Science Foundation (NSF) under grant AGS-1122989, Takenaka Scholarship Foundation, Iizuka Takeshi Scholarship Foundation, and the NSF under grant AGS-0960497. We thank Steve Warren and Cecilia Bitz for helpful discussion and Peter Blossey for sharing the RRTMG code. We also thank the CALIPSO team for making the data readily available and the authors of [Chepfer et al., 2010] for creating the GOCCP dataset. We acknowledge the World Climate Research Programme's Working Group on Coupled Modelling, which is responsible for CMIP, and we thank the climate modeling groups for producing and making available their model output. For CMIP the U.S. Department of Energy's Program for Climate Model Diagnosis and Intercomparison provides coordinating support and led development of software infrastructure in partnership with the Global Organization for Earth System Science Portals.

Appendix

Derivation of 95% confidence interval for the mean low cloud fraction

The mean low cloud fraction (LCF) as a function of meridional distance from the sea ice edge for the Weddell Sea is shown in Figure 3b, Figure 12 and Table 1, and for the Ross Sea in Figure 3g. The 95% confidence interval for mean LCF was computed assuming that the LCF measured at each grid cell and time is independent. The LCF data is available as monthly averages on a 2°×2° (longitude, latitude) grid. To justify the assumption that measurements of LCF at each grid cell and time are independent we must assess spatial and temporal autocorrelation.

- *Serial correlation in the meridional dimension*

Our goal is to bin the data by meridional distance from the ice edge and compute the mean and 95% confidence interval for the mean of each bin. The CALIPSO grid is resolved in 2° latitude grid cells, and when compositing by meridional distance from the ice edge we use bins of width 0.5° latitude. Therefore, for any given time, no two grid cells of the same longitude and neighboring latitudes can be assigned to the same bin. We therefore do not need to consider serial correlation in the meridional dimension when estimating the effective degrees of freedom of each bin.

- *Serial correlation in the zonal dimension*

We estimate a lower bound for the number of degrees of freedom in the zonal dimension by computing the correlation length scale L for each latitude and time, and comparing it to the resolution of the CALIPSO grid. Following [Taylor, 1921; Keller, 1935], we define the correlation length scale as

$$L = \int_0^\infty r(\tau) d\tau$$

where $r(\tau)$ is the spatial autocorrelation function of LCF in the zonal dimension and τ is the separation distance. The distance between independent points in the zonal dimension can be thought of as $2L$. For each time and latitude within 10 degrees of the sea ice edge we computed $2L$, and the maximum value was an order of magnitude smaller than the 2° longitude resolution of the CALIPSO grid. We therefore treat each grid cell as an independent measurement of LCF in the zonal dimension.

- *Serial correlation in the time dimension*

Each longitude and latitude grid cell contains a timeseries of LCF observations, and the number of effective degrees of freedom of the LCF timeseries (N_{eff}) is related to the number observations of LCF (N) and the lag-1 autocorrelation of LCF (r_1) by the following equation [Bretherton et al., 1999]:

$$\frac{N_{eff}}{N} = \frac{1 - r_1}{1 + r_1}$$

525

526 Our goal is to bin the observations of LCF by their meridional distance from the ice
527 edge and then to use this equation to estimate the effective degrees of freedom for
528 each bin. For each longitude and latitude grid cell we compute r_1 over the entire
529 timeseries. Then, for a given bin, say "bin A," and a given grid cell, say "grid cell B,"
530 we keep track of the number of times that grid cell B is assigned to bin A and then
531 compute an estimate for the number of effective degrees of freedom contributed to
532 bin A by grid cell B by scaling by the right hand side of the above equation. This
533 procedure was repeated for every grid cell and every bin.
534

535 The total number of effective degrees of freedom for each bin estimated by this
536 procedure is slightly greater than if one were to assume each observation of LCF is
537 independent in the time dimension. This happens because the lag-1 autocorrelation
538 of LCF over the domain tends to be slightly negative. We therefore assume that each
539 estimate of LCF is independent in the time dimension.

References

Abbot, D. S., & Tziperman, E. (2008). Sea ice, high-latitude convection, and equable climates. *Geophysical Research Letters*, *35*(3), 1–5. doi:10.1029/2007GL032286

Ackerman, S. a., Holz, R. E., Frey, R., Eloranta, E. W., Maddux, B. C., & McGill, M. (2008). Cloud detection with MODIS. Part II: Validation. *Journal of Atmospheric and Oceanic Technology*, *25*(7), 1073–1086. doi:10.1175/2007JTECHA1053.1

Andreas, E. L., Claffey, K. J., & Makshtas, a. P. (2000). Low-level atmospheric jets and inversions over the western Weddell Sea. *Boundary-Layer Meteorology*, *97*(3), 459–486. doi:10.1023/A:1002793831076

Blackadar, A. K.: 1957, Boundary Layer Wind Maxima and their Significance for the Growth of Nocturnal Inversions, Bull. Amer. Meteorol. Soc. 38, 283–290.

Boisvert, L. N., & Stroeve, J. C. (2015). The Arctic is becoming warmer and wetter as revealed by the Atmospheric Infrared Sounder, *Geophysical Research Letters* 4439–4446. doi:10.1002/2015GL063775

Bretherton, C. S., Widmann, M., Dymnikov, V. P., Wallace, J. M., & Blade, I. (1999). Effective number of degrees of freedom of a spatial field. *Journal of Climate*, *12*(1969), 1990–2009. doi:10.1175/1520-0442(1999)012<1990:Tenosd>2.0.Co;2

Bromwich, D. H., Nicolas, J. P., Hines, K. M., Kay, J. E., Key, E. L., Lazzara, M. a., … Van Lipzig, N. P. M. (2012). Tropospheric clouds in Antarctica. *Reviews of Geophysics*, *50*(1), 1–40. doi:10.1029/2011RG000363

559 CALIPSO, 2015: GOCCP, Subset: Monthly, June, 2006-August, 2014. CFMIP-Obs: Cloud Observations
560 for Model Evaluation. Accessed 1 January, 2016. [available online at
561 http://climserv.ipsl.polytechnique.fr/cfmip-obs/]

562 Chepfer, H., Bony, S., Winker, D., Chiriaco, M., Dufresne, J. L., & Sèze, G. (2008). Use of CALIPSO lidar
563 observations to evaluate the cloudiness simulated by a climate model. *Geophysical Research Letters*,
564 *35*(15), 1–6. doi:10.1029/2008GL034207

565 Chepfer, H., Bony, S., Winker, D., Cesana, G., Dufresne, J. L., Minnis, P., … Zeng, S. (2010). The GCM-
566 oriented CALIPSO cloud product (CALIPSO-GOCCP). *Journal of Geophysical Research*
567 *Atmospheres*, *115*(5), 1–13. doi:10.1029/2009JD012251

568 Clough, S.A., M.W. Shephard, E.J. Mlawer, J.S. Delamere, M.J. Iacono, K. Cady-Pereira, S. Boukabara,
569 P.D. Brown, (2005). Atmospheric radiative transfer modeling: a summary of the AER codes, *J.*
570 *Quant. Spectrosc. Radiat. Transfer.*, **91**, 233-244

571 Dee, D. P., Uppala, S. M., Simmons, a. J., Berrisford, P., Poli, P., Kobayashi, S., … Vitart, F. (2011). The
572 ERA-Interim reanalysis: Configuration and performance of the data assimilation system. *Quarterly*
573 *Journal of the Royal Meteorological Society*, *137*(April), 553–597. doi:10.1002/qj.828

574 Dong, S., Sprintall, J., Gille, S. T., & Talley, L. (2008). Southern ocean mixed-layer depth from Argo float
575 profiles. *Journal of Geophysical Research: Oceans*, *113*(6), 1–12. doi:10.1029/2006JC004051

576 Dufresne, J. L., & Bony, S. (2008). An assessment of the primary sources of spread of global warming
577 estimates from coupled atmosphere-ocean models. *Journal of Climate*, *21*(19), 5135–5144.
578 doi:10.1175/2008JCLI2239.1

579 Eastman, R., & Warren, S. G. (2010). Interannual variations of arctic cloud types in relation to sea ice.
580 *Journal of Climate*, *23*(15), 4216–4232. doi:10.1175/2010JCLI3492.1

ECMWF, 2015: ERA-Interim Project. Subset: Monthly, June 2006-August 2014. Accessed 1 January, 2016. [available online at http://apps.ecmwf.int/datasets/]

Elsaesser, G., C. O'Dell, and J. Teixeira (2015). Algorithm Theoretical Basis Document (ATBD) Version 1: Multi-Sensor Advanced Climatology of Liquid Water Path (MAC-LWP). An Enhanced Climate Data Record (CDR) for MEaSUREs Project "A Data Record of the Cloudy Boundary Layer". 20 pps.

Fitzpatrick, M. F., & Warren, S. G. (2007). The Relative Importance of Clouds and Sea Ice for the Solar Energy Budget of the Southern Ocean. *Journal of Climate*, *20*(6), 941–954. doi:10.1175/JCLI4040.1

Gates, W. L. (1992), AMIP: The Atmospheric Model Intercomparison Project. *Bull. Amer. Meteor. Soc.*, 73, 1962-1970

Gordon, A. L. (1991), Two stable modes of Southern Ocean winter stratification, in Deep Convection and Deep Water Formation in the Oceans, Elsevier Oceanogr. Ser., vol. 57, edited by P. C. Chu and J. C. Gascard, pp. 17–35, Elsevier, New York.

Gordon, A. L., & Ice Station Weddell Group of Principal Investigators and Chief Scientists (1993). Weddell Sea exploration from ice station. *Eos, Transactions, American Geophysical Union*, *74*(11), 121,124–126.

Hartmann, D. L. (2016). *Global Physical Climatology, Second Ed.*, 77 pp., Academic Press, Amsterdam

Hu, Y., Rodier, S., Xu, K. M., Sun, W., Huang, J., Lin, B., … Josset, D. (2010). Occurrence, liquid water content, and fraction of supercooled water clouds from combined CALIOP/IIR/MODIS measurements. *Journal of Geophysical Research: Atmospheres*, *115*(19), 1–13. doi:10.1029/2009JD012384

603 Iacono, M.J., J.S. Delamere, E.J. Mlawer, M.W. Shephard, S.A. Clough, and W.D. Collins, (2008).
604 Radiative forcing by long-lived greenhouse gases: Calculations with the AER radiative transfer
605 models, *J. Geophys. Res.*, **113**, D13103, doi:10.1029/2008JD009944

606 Ice Station Weddell, 1993. Atmospheric Boundary Layer Measurements on the Weddell Sea Drifting
607 Station. Antarctic Master Directory. Accessed 1 March, 2016. [available online at
608 http://gcmd.gsfc.nasa.gov/search/Metadata.do?entry=NSF-ANT90-24544#metadata]

609 Kapsch, M.-L., Graversen, R. G., & Tjernström, M. (2013). Springtime atmospheric energy transport and
610 the control of Arctic summer sea-ice extent. *Nature Climate Change*, *3*(8), 744–748.
611 doi:10.1038/nclimate1884

612 Kay, J. E., & Gettelman, A. (2009). Cloud influence on and response to seasonal Arctic sea ice loss.
613 *Journal of Geophysical Research Atmospheres*, *114*(18), 1–18. doi:10.1029/2009JD011773

614 Keller, L. B., 1935: Expanding of limit theorems of probability theory on functions with continuous
615 arguments (in Russian). Works Main Geophys. Observ., 4, 5–19. Kikkawa,

616 König-Langlo, Gert (2013): Meteorological observations during POLARSTERN cruise ANT-XXIX/6
617 (AWECS). *Alfred Wegener Institute, Helmholtz Center for Polar and Marine Research,*
618 *Bremerhaven*, doi:10.1594/PANGAEA.819610 [available online at
619 https://pangaea.de/PHP/CruiseReports.php?b=Polarstern]

620 König-Langlo, G., Loose, B., & Bräuer, B. (2006). 25 Years of Polarstern Meteorology. *WDC-MARE*
621 *Reports*. doi:10.2312/wdc-mare.2006.4

622 Kurtz, N. T., & Markus, T. (2012). Satellite observations of Antarctic sea ice thickness and volume.
623 *Journal of Geophysical Research: Oceans*, *117*(8), 1–9. doi:10.1029/2012JC008141

624 Leibowicz, B. D., D. S. Abbot, K. Emanuel, and E. Tziperman (2012), Correlation between present-day
625 model simulation of Arctic cloud radiative forcing and sea ice consistent with positive winter
626 convective cloud feedback, *J. Adv. Model. Earth Syst.*, 4, M07002, doi:10.1029/2012MS000153.

627 Liu, Y., Key, J. R., Frey, R. a., Ackerman, S. a., & Menzel, W. P. (2004). Nighttime polar cloud detection
628 with MODIS. *Remote Sensing of Environment*, *92*(2), 181–194. doi:10.1016/j.rse.2004.06.004

629 Mccoy, D. T., Hartmann, D. L., & Grosvenor, D. P. (2014). Observed Southern Ocean Cloud Properties
630 and Shortwave Reflection Part I : Calculation of SW flux from observed cloud. *Journal of Climate*,
631 *27*, 8836–8857. doi:10.1175/JCLI-D-14-00287.1

632 Mlawer, E.J., S.J. Taubman, P.D. Brown, M.J. Iacono and S.A. Clough (1997). RRTM, a validated
633 correlated-k model for the longwave. *J. Geophys. Res.*, **102**, 16,663-16,682

634 Morrison, A. E., Siems, S. T., & Manton, M. J. (2011). A three-year climatology of cloud-top phase over
635 the Southern Ocean and North Pacific. *Journal of Climate*, *24*, 2405–2418.
636 doi:10.1175/2010JCLI3842.1

637 Nicolas, J. P., & Bromwich, D. H. (2011). Climate of West Antarctica and influence of marine air
638 intrusions. *Journal of Climate*, *24*(1), 49–67. doi:10.1175/2010JCLI3522.1

639 NOAA/NSIDC Climate Data Record of Passive Microwave Sea Ice Concentration, Version 2, 2015.
640 Subset: Monthly, June 2006-August, 2014. National Snow and Ice Data Center, accessed 1 January,
641 2016. [available online at https://nsidc.org/data]

642 Palm, S. P., Strey, S. T., Spinhirne, J., & Markus, T. (2010). Influence of Arctic sea ice extent on polar
643 cloud fraction and vertical structure and implications for regional climate. *J. Geophys. Res.*,
644 *115*(D21), D21209–. doi:10.1029/2010JD013900

645 Parish, T. R. (1983). The Influence of the Antarctica Peninsula on the Wind Field Over the Western
646 Weddell Sea. *Journal of Geophysical Research*, *88*, 2684–2692.

647 Peng, G., Meier, W. N., Scott, D. J., & Savoie, M. H. (2013). A long-term and reproducible passive
648 microwave sea ice concentration data record for climate studies and monitoring. *Earth System*
649 *Science Data*, *5*(2), 311–318. doi:10.5194/essd-5-311-2013

650 Rienecker, M. M., and Coauthors, 2011: MERRA: NASA's Modern-Era Retrospective Analysis for
651 Research and Application. J. Climate, 24, 3624–3648, doi:10.1175/ JCLI-D-11-00015.1.

652 Schweiger, A. J., Lindsay, R. W., Vavrus, S., & Francis, J. a. (2008). Relationships between Arctic sea ice
653 and clouds during autumn. *Journal of Climate*, *21*(18), 4799–4810. doi:10.1175/2008JCLI2156.1

654 Schwerdtfeger, W. (1979). Meteorological Aspects of the Drift of Ice From the Weddell Sea Toward the
655 Mid-Latitude Westerlies. *Journal of Geophysical Research*, *84*(C10), 6321–6328.
656 doi:10.1029/JC084iC10p06321

657 Taylor, G. I., 1921: Diffusion by continuous movement. Proc. London Math. Soc., 20 (2), 196–212.

658 Taylor, K. E., Stouffer, R. J., & Meehl, G. a. (2012). An overview of CMIP5 and the experiment design.
659 *Bulletin of the American Meteorological Society*, *93*(4), 485–498. doi:10.1175/BAMS-D-11-00094.1

660 Thorndike, A. S. (1992). A Toy Model Linking Atmospheric Thermal Radiation and Sea Ice Growth.
661 *Journal of Geophysical Research: Oceans*, 97(6), 9401-9410. doi:10.1029/92JC00695

662 Thorpe, A. J. and Guymer, T. H.: 1977, 'The Nocturnal Jet', Quart. J. Roy. Meteorol. Soc. 103, 633–653.

663 Trenberth, K. E., & Fasullo, J. T. (2010). Simulation of present-day and twenty-first-century energy
664 budgets of the southern oceans. *Journal of Climate*, *23*, 440–454. doi:10.1175/2009JCLI3152.1

665 Wadhams, P., Lange, M. a, & Ackley, S. F. (1987). The ice thickness distribution across the Atlantic sector
666 of the Antarctic Ocean in midwinter. *Journal of Geophysical Research: Oceans (1978--2012)*,
667 *92*(C13), 14535–14552.

668 Winker, D. M., Hunt, W. H., & McGill, M. J. (2007). Initial performance assessment of CALIOP.
669 *Geophysical Research Letters*, *34*(19), 1–5. doi:10.1029/2007GL030135

670

Table Captions

Table 1. Mean and 95% confidence interval for various observed and computed values over the "open water" and "sea ice" composites (1°-3° equatorward and 2°-4° poleward of the sea ice edge, respectively) during JJA in the Weddell Sea.

Figure Captions

Figure 1. 2006-2014 climatology of June, July and August cloud incidence between 0.96-1.44 km (color) and the 35% sea ice concentration contour (black line).

Figure 2. (a) Map of region analyzed, (b) mean vertical profile of cloud incidence observed by CALIPSO, (c) mean SIC and mean and 95% confidence interval of LCF (see Appendix), and (d) mean vertical profile of potential temperature (contours) and specific humidity (color) over the Weddell Sea during JJA as a function of meridional distance from the ice edge. (e-h) as in (a-d) but for the Ross Sea.

Figure 3. Cruise track and Ice Station Weddell (on which surface heat budget measurements were made) drift path during the period of study. The cruise traversed from west to east and the Ice Station Weddell drifted from south to north. The green dot shows the location of the sounding shown in Figure 5.

Figure 4. Vertical temperature profile of the lower troposphere over the Weddell Sea during winter from soundings. For each height, color shows the probability density function of air temperature from soundings taken between 60-65°S (a) and poleward of 65°S (b). Bins of width 2°C were used in the calculation. The black dashed line shows a moist adiabat with a surface temperature of -1.8°C, the approximate freezing temperature of seawater in the Southern Ocean. Twenty-five soundings were used in both (a) and (b).

Figure 5. Observed low-level jets from soundings taken over the Weddell Sea. (a) One sounding showing an example of a low-level jet and inversion. See Figure 3 for the location at which this sounding was obtained. (b) Speed and direction of the low-level jet core for all observed jets.

Figure 6. Hourly-average measurements of the surface energy budget over a drifting ice floe in the Weddell Sea during April-May, 1992. Individual heat budget terms are shown in (a), including absorbed SW radiation (SW_{abs}), surface latent and sensible heat fluxes (H_L and H_S respectively), upward and downward LW fluxes, and net heat flux. Terms are defined to be positive when heat flows into the ice. The box center line (edges) show the median (25- and 75-percentiles), while the whiskers show the 5- and 95-percentiles. The LW terms are shown in (b). The black line is the one-to-one line, while the red line and shading shows the mean and 95% confidence interval of the mean upward LW flux as function of downward LW flux. See text for a description of how this was computed.

714

715 **Figure 7.** Temperature (a), specific humidity (b), and LWP (c) values used in the
716 radiative transfer calculations. Blue (gray) color denotes profiles from the "open
717 water" ("sea ice") composites. In (a) and (b), thick center lines show the mean value,
718 while the edges of the dark (light) shading show the 25- and 75- (5- and 95-)
719 percentiles at each height. LWP observations shown in (c) are from the "open water"
720 composite.

721

722 **Figure 8.** Computed surface downward LW fluxes. Clear-sky fluxes for the "sea ice"
723 (gray) and "open water" (blue) composites are shown in (a). The box center line
724 (edges) shows the median (25- and 75-percentiles), and whiskers correspond to the
725 5- and 95-percentiles. Surface LW CRE* as a function of condensed water path is
726 shown in (b). The mean and 95% confidence interval for all scenes in the "open
727 water" composite are shown in blue. Values for low liquid and ice clouds over the
728 "sea ice" composite are shown in dark and light gray, respectively. The light gray
729 line (shading edges) shows the values for a liquid cloud with a droplet effective
730 radius of 16 μm (12-20 μm). The dark gray line (shading edges) shows the values
731 for an ice cloud with ice crystal effective radius of 30 μm (20-40 μm).

732

733 **Figure 9.** JJA-mean cloud incidence for the 0.96-1.44 km layer (color) and ice edge
734 (contour) for seven fully coupled CMIP5 models with CALIPSO simulators and
735 observations ("OBS").

736

737 **Figure 10.** As in Figure 9 but for models in AMIP configuration. Note that only three
738 models shown here also have output from their fully coupled configuration shown
739 in Figure 9 (HadGEM2-A, MPI-ESM-LR, MIROC5).
740
741 **Figure 11.** Mean LCF during JJA in the Weddell Sea as a function of meridional
742 distance from the sea ice edge for models in fully coupled and AMIP configurations
743 and observations. Solid lines show models that have both fully coupled and AMIP
744 output. Error bars on observations show the 95% confidence interval (see
745 Appendix).
746

Tables

Composite	Surface $LW_{\downarrow,clear}$ (W/m^2)	Surface LW CRE* (W/m^2)	LWP (g/m^2)	CALIPSO LCF	Temperature/ Humidity
"open water"	200.5 ± 0.5	87.3 ± 0.1	79 ± 2	0.69 ± 0.01	See Figure 8
"sea ice"	176.1 ± 0.7	-	-	0.52 ± 0.01	

Table 1. Mean and 95% confidence interval for various observed and computed values over the "open water" and "sea ice" composites (1°-3° equatorward and 2°-4° poleward of the sea ice edge, respectively) during JJA in the Weddell Sea.

754 # Figures

755

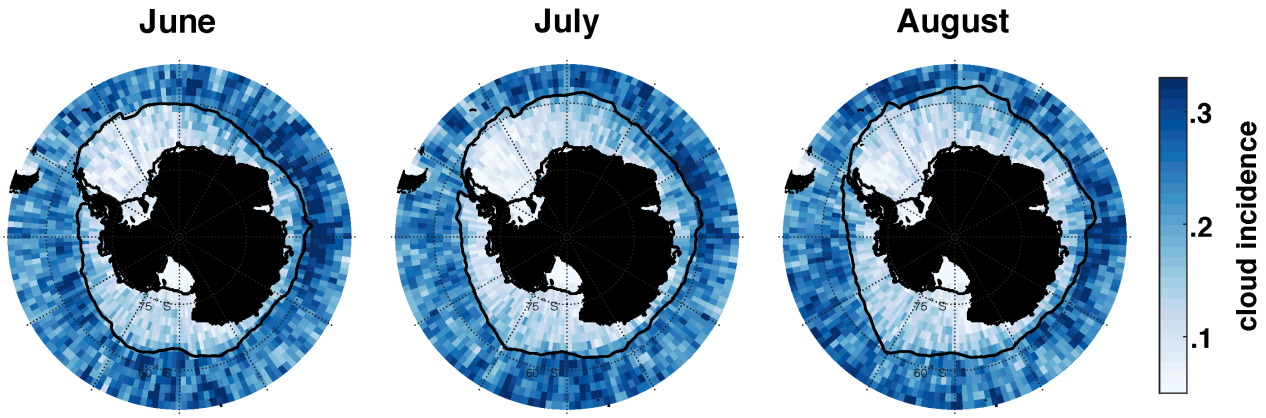

757

758 **Figure 1.** 2006-2014 climatology of June, July and August cloud incidence between

759 0.96-1.44 km (color) and the 35% sea ice concentration contour (black line).

760

761

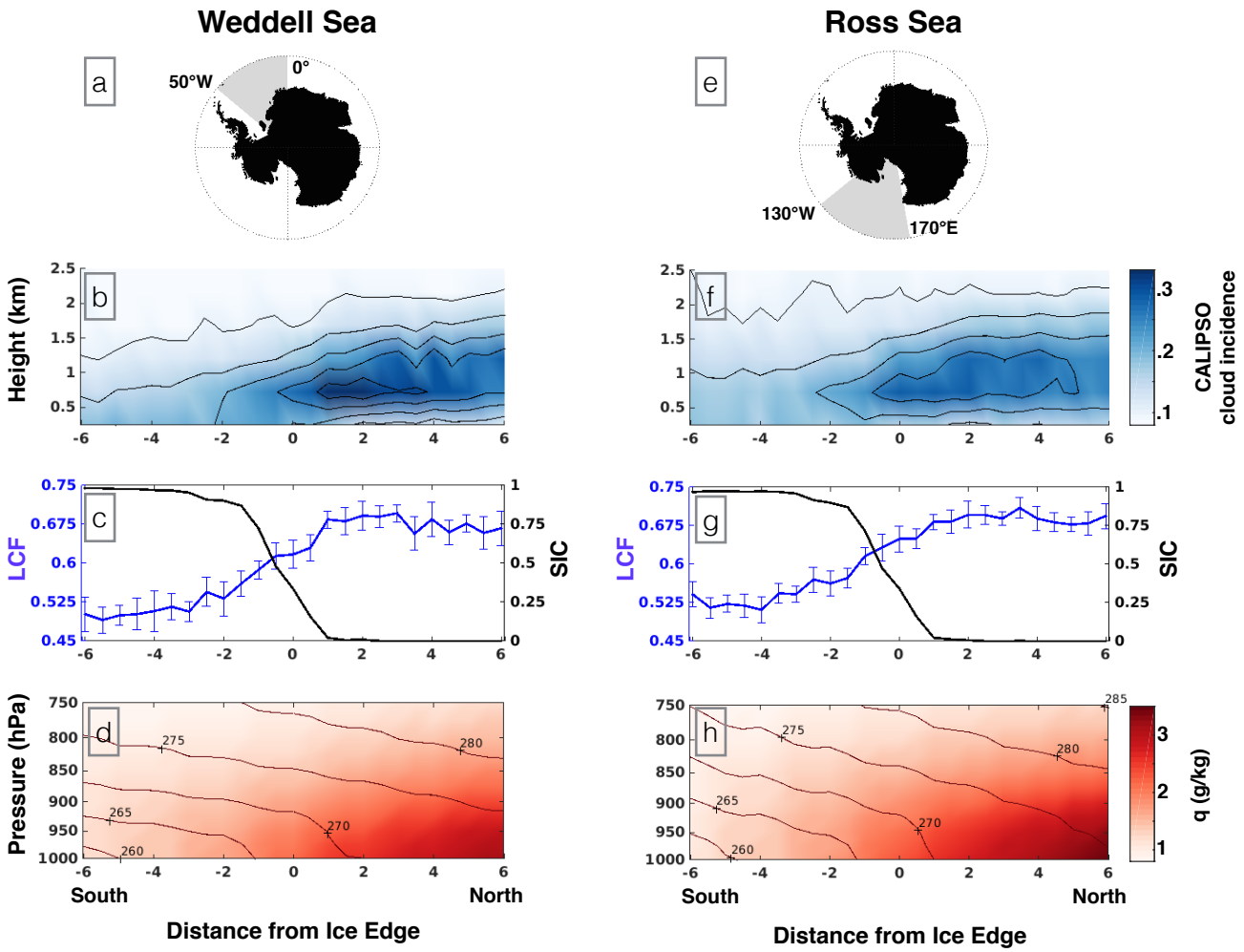

763 **Figure 2.** (a) Map of region analyzed, (b) mean vertical profile of cloud incidence
764 observed by CALIPSO, (c) mean SIC and mean and 95% confidence interval of LCF
765 (see Appendix), and (d) mean vertical profile of potential temperature (contours)
766 and specific humidity (color) over the Weddell Sea during JJA as a function of
767 meridional distance from the ice edge. (e-h) as in (a-d) but for the Ross Sea.

768

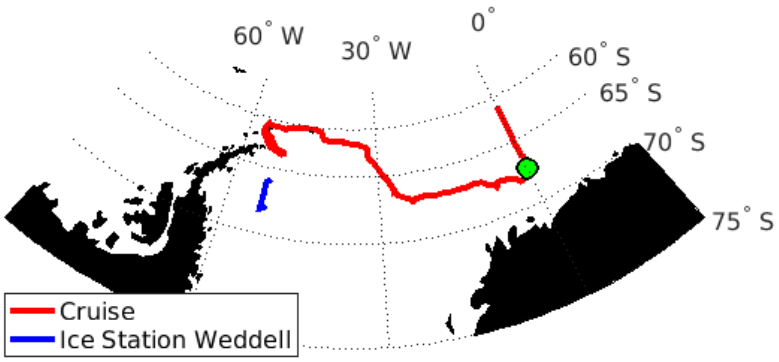

Figure 3. Cruise track and Ice Station Weddell (on which surface heat budget measurements were made) drift path during the period of study. The cruise traversed from west to east and the Ice Station Weddell drifted from south to north. The green dot shows the location of the sounding shown in Figure 5.

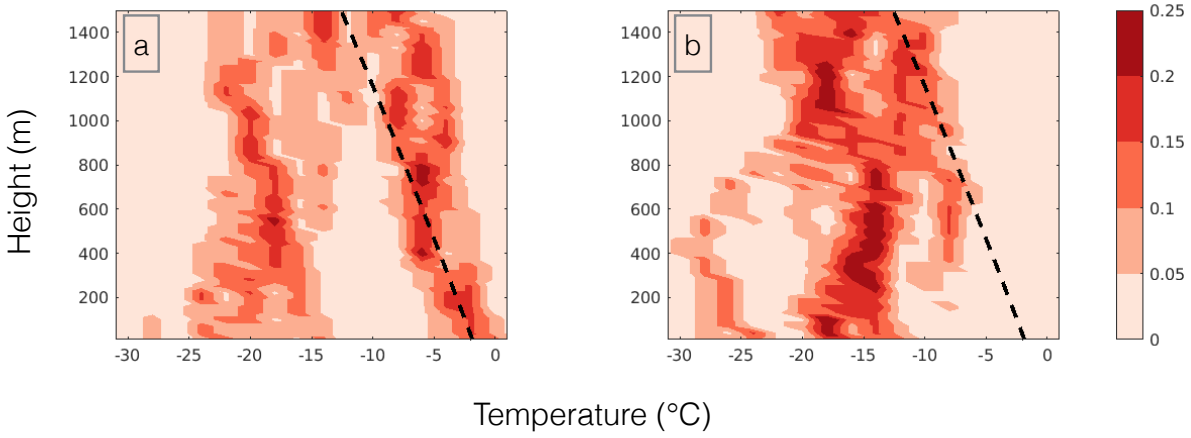

Figure 4. Vertical temperature profile of the lower troposphere over the Weddell Sea during winter from soundings. For each height, color shows the probability density function of air temperature from soundings taken between 60-65°S (a) and poleward of 65°S (b). Bins of width 2°C were used in the calculation. The black dashed line shows a moist adiabat with a surface temperature of -1.8°C, the approximate freezing temperature of seawater in the Southern Ocean. Twenty-five soundings were used in both (a) and (b).

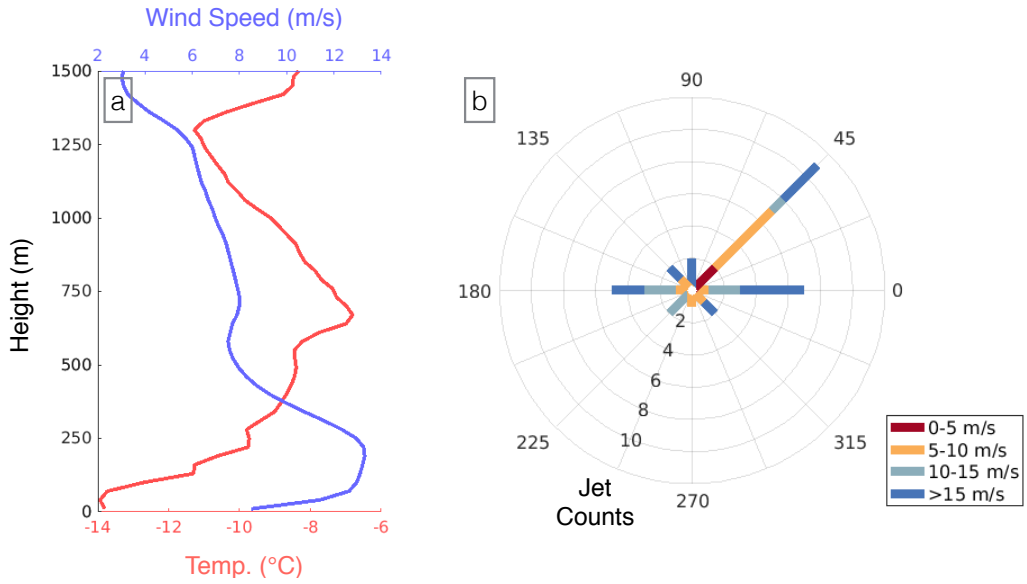

Figure 5. Observed low-level jets from soundings taken over the Weddell Sea. (a) One sounding showing an example of a low-level jet and inversion. See Figure 3 for the location at which this sounding was obtained. (b) Speed and direction of the low-level jet core for all observed jets.

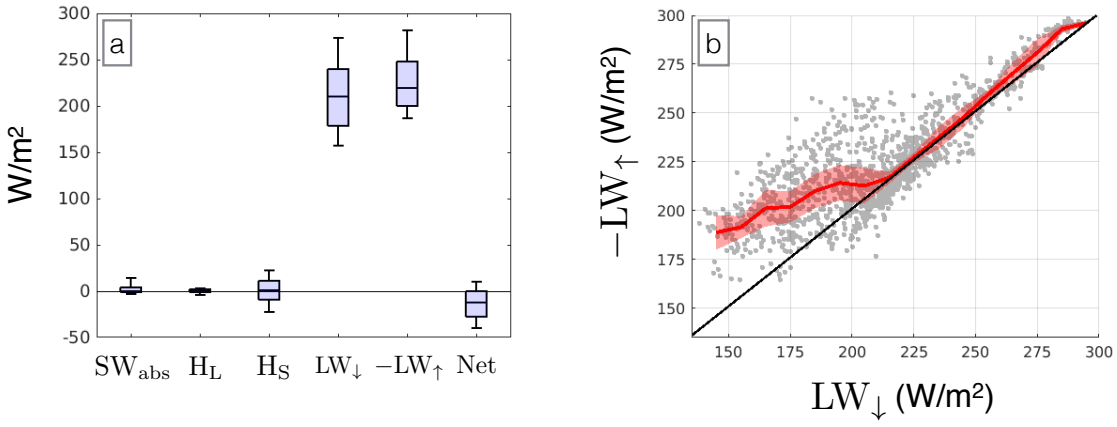

Figure 6. Hourly-average measurements of the surface energy budget over a drifting ice floe in the Weddell Sea during April-May, 1992. Individual heat budget terms are shown in (a), including absorbed SW radiation (SW_{abs}), surface latent and sensible heat fluxes (H_L and H_S respectively), upward and downward LW fluxes, and net heat flux. Terms are defined to be positive when heat flows into the ice. The box center line (edges) show the median (25- and 75-percentiles), while the whiskers show the 5- and 95-percentiles. The LW terms are shown in (b). The black line is the one-to-one line, while the red line and shading shows the mean and 95% confidence interval of the mean upward LW flux as function of downward LW flux. See text for a description of how this was computed.

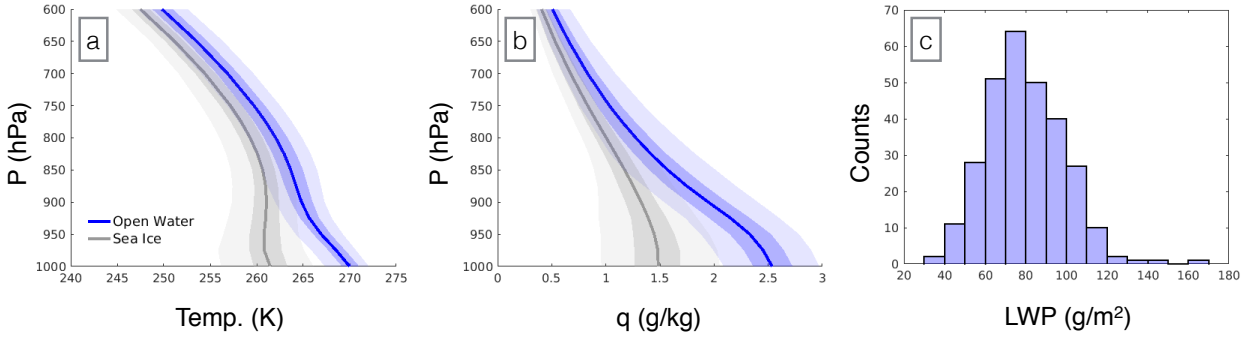

Figure 7. Temperature (a), specific humidity (b), and LWP (c) values used in the radiative transfer calculations. Blue (gray) color denotes profiles from the "open water" ("sea ice") composites. In (a) and (b), thick center lines show the mean value, while the edges of the dark (light) shading show the 25- and 75- (5- and 95-) percentiles at each height. LWP observations shown in (c) are from the "open water" composite.

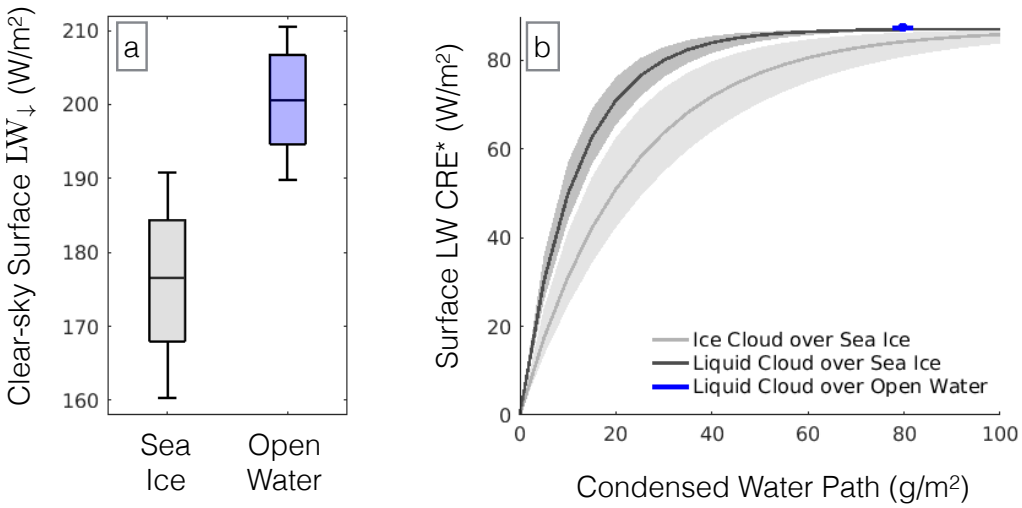

Figure 8. Computed surface downward LW fluxes. Clear-sky fluxes for the "sea ice" (gray) and "open water" (blue) composites are shown in (a). The box center line (edges) shows the median (25- and 75-percentiles), and whiskers correspond to the 5- and 95-percentiles. Surface LW CRE* as a function of condensed water path is shown in (b). The mean and 95% confidence interval for all scenes in the "open water" composite are shown in blue. Values for low liquid and ice clouds over the "sea ice" composite are shown in dark and light gray, respectively. The light gray line (shading edges) shows the values for a liquid cloud with a droplet effective radius of 16 μm (12-20 μm). The dark gray line (shading edges) shows the values for an ice cloud with ice crystal effective radius of 30 μm (20-40 μm).

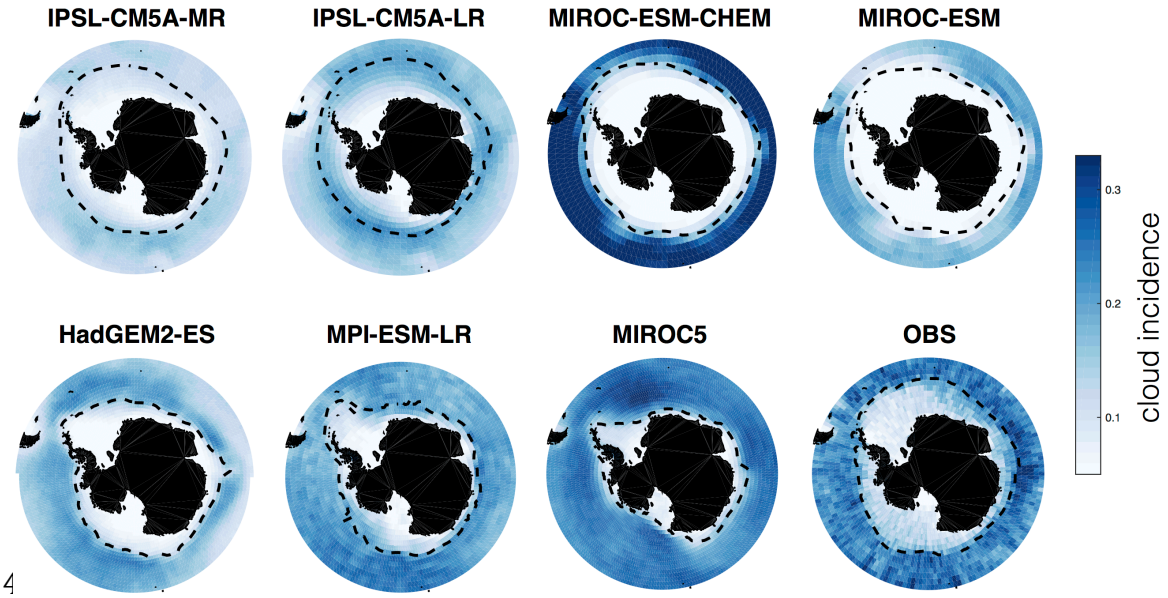

Figure 9. JJA-mean cloud incidence for the 0.96-1.44 km layer (color) and ice edge (contour) for seven fully coupled CMIP5 models with CALIPSO simulators and observations ("OBS").

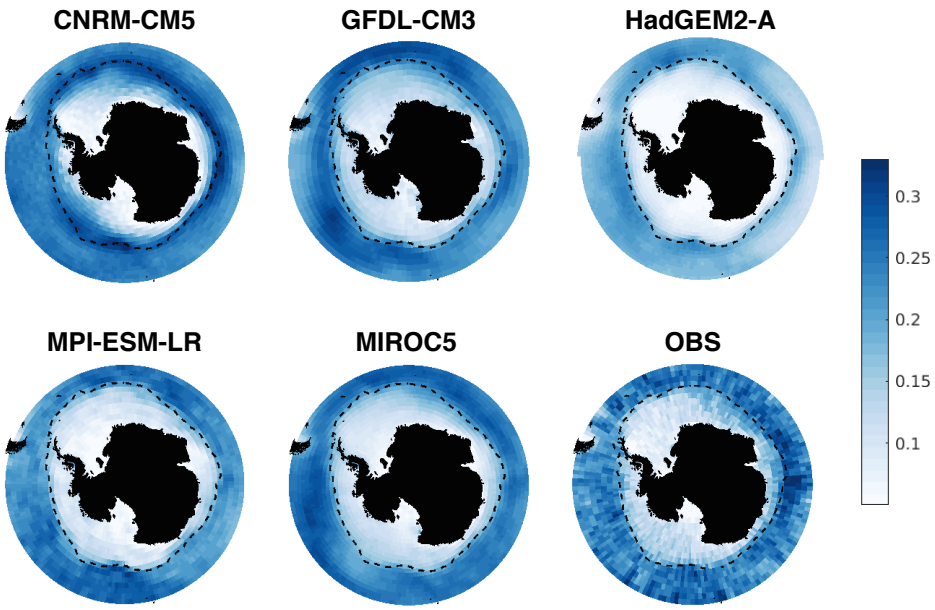

Figure 10. As in Figure 9 but for models in AMIP configuration. Note that only three models shown here also have output from their fully coupled configuration shown in Figure 9 (HadGEM2-A, MPI-ESM-LR, MIROC5).

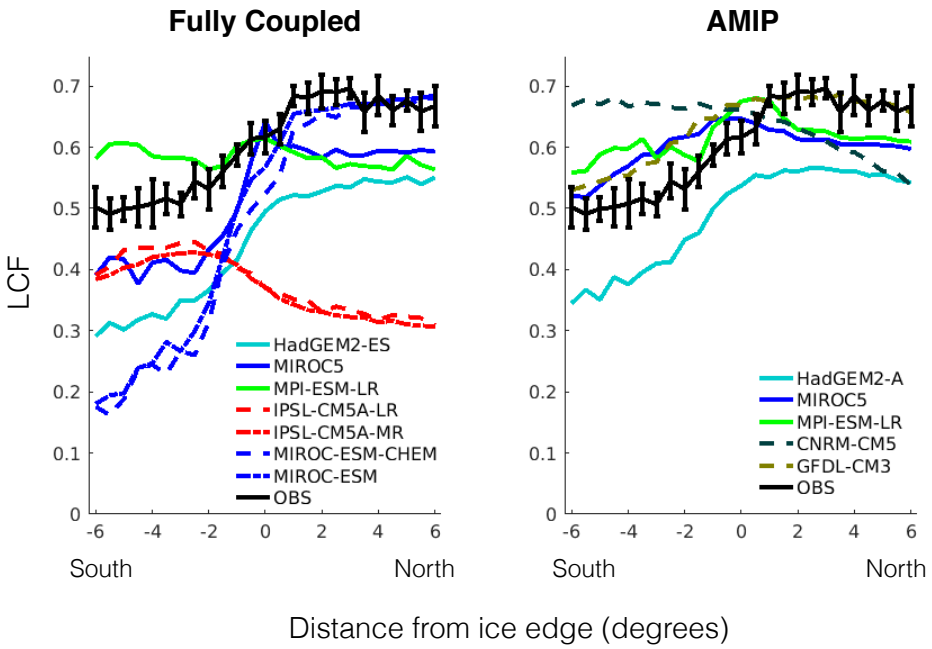

847

848

849 **Figure 11.** Mean LCF during JJA in the Weddell Sea as a function of meridional

850 distance from the sea ice edge for models in fully coupled and AMIP configurations

851 and observations. Solid lines show models that have both fully coupled and AMIP

852 output. Error bars on observations show the 95% confidence interval (see

853 Appendix).

854